

Seismicity under a Dormant Volcano: Unveiling Active Crustal Faulting beneath Piton des Neiges, La Réunion

Lise Firode^{*1}, Zacharie Duputel¹, Valérie Ferrazzini¹, and Olivier Lengliné²

ABSTRACT

Volcanic environments are commonly associated with seismic activity. The two prominent shield volcanoes of La Réunion island—Piton des Neiges and Piton de la Fournaise, exhibit sustained seismic activity. Whereas the seismicity at Piton de la Fournaise is tied to its volcanic activity, the seismic activity beneath Piton des Neiges, which has been dormant for 27,000 yr, remains poorly understood. The occurrence of earthquakes under the north flank of Piton des Neiges, often felt by the population, led to the deployment of several seismic stations in the area since 2012. In this study, we employ template matching and double-difference relocation techniques to construct a high-resolution catalog of the region. Our results reveal that the seismicity observed under Piton des Neiges is primarily concentrated on a northeast-dipping fault located in the oceanic crust beneath the volcanic edifice. Analysis of focal mechanisms indicates that this structure operates as a reverse fault. In the vicinity of this primary fault, we also identify secondary seismicity clusters with similar orientation and focal mechanisms. The region has experienced continuous seismicity since 1999, with occasional periods of increased swarmlike activity in 2011 and 2018. These fluctuations in seismicity rate do not correlate with markers of deep magma transfers often observed before eruptions at the Piton de la Fournaise volcano. Beyond the crustal faults highlighted in this study, it is noteworthy that the majority of earthquakes in northern La Réunion island exhibit consistent reverse focal mechanisms. These observations suggest that seismic events may not be driven by deep magmatic activity but, rather, result from regional tectonic stress and edifice loading on pre-existing faults.

KEY POINTS

- We characterize seismic activity beneath Piton des Neiges volcano, which has been dormant for 27,000 yr.
- We identify a main reverse fault along with secondary structures in the oceanic crust below the edifice.
- The primary fault has been active since 1999 with intermittent swarm-like activity in 2011 and 2018.

Supplemental Material

volcanotectonic (VT) seismicity is often observed on faults around dormant stratovolcanoes before their reactivation (White and McCausland, 2016, 2019; Nunez *et al.*, 2022). Moreover, the evolution of long-period (LP) seismicity can reflect pressure fluctuations in magmatic and hydrothermal fluids and thus reveals magmatic intrusion (Chouet, 2003; Chouet and Matoza, 2013; Frank *et al.*, 2018; Kugaenka *et al.*, 2021). The recording of periodic or quasi-periodic seismicity beneath dormant volcanoes may also indicate residual degassing processes (Lin, 2017) or magma cooling (Wech *et al.*, 2020). Analyzing seismicity can also yield

INTRODUCTION

Seismic activity is a primary source of information for understanding the nature and evolution of volcanoes (McNutt, 2005; Lemarchand and Grasso, 2007; Brenguier *et al.*, 2011; Sparks *et al.*, 2012). Although most studies focus on the seismicity of active volcanic areas, it is also important to monitor dormant volcanoes, which can rapidly reactivate after a long period of quiescence (Gottsmann *et al.*, 2006; Konstantinou *et al.*, 2007; Feuillet *et al.*, 2021; Longpré, 2021). Seismicity frequently offers early indications of an impending reactivation. For example,

1. Observatoire Volcanologique du Piton de la Fournaise, Institut de physique du globe de Paris, Université Paris Cité, Paris, France, <https://orcid.org/0009-0002-8659-3195> (LF); <https://orcid.org/0000-0002-8809-451X> (ZD); <https://orcid.org/0000-0001-7908-1429> (VF); 2. Institut Terre et Environnement de Strasbourg (ITES), Université de Strasbourg, CNRS, Strasbourg, France, <https://orcid.org/0000-0003-0678-2587> (OL)

*Corresponding author: firode@ipgp.fr

Cite this article as Firode, L., Z. Duputel, V. Ferrazzini, and O. Lengliné (2024). Seismicity under a Dormant Volcano: Unveiling Active Crustal Faulting beneath Piton des Neiges, La Réunion, *Bull. Seismol. Soc. Am.* **114**, 1626–1638, doi: [10.1785/0120230284](https://doi.org/10.1785/0120230284)

© Seismological Society of America

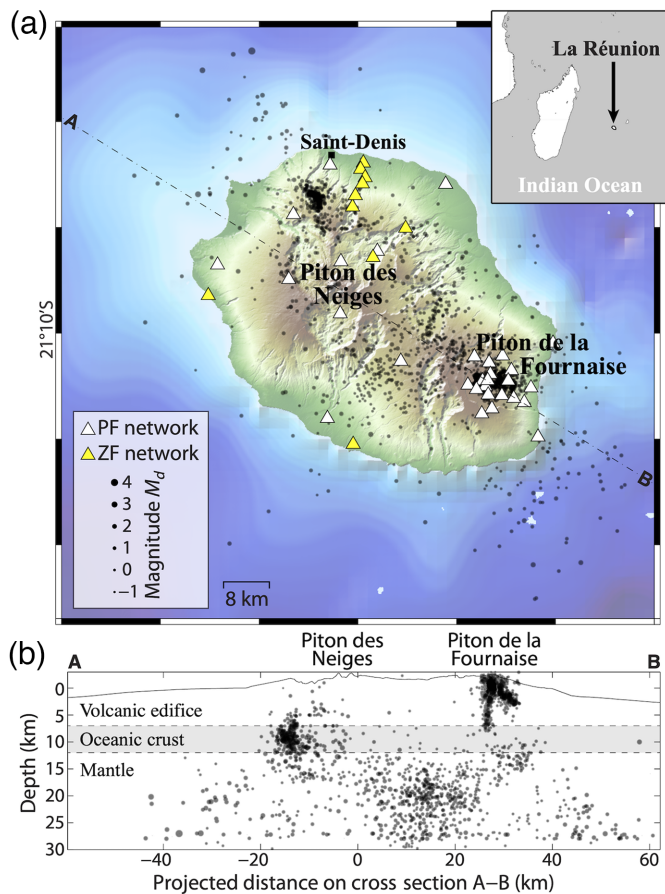


Figure 1. Seismicity and seismological network of La Réunion island. (a) Events detected and located by Observatoire Volcanologique du Piton de la Fournaise (OVPF) from January 2013 until September 2022 are represented by black dots and are scaled according to their magnitude. Seismological stations are represented by triangles, the color indicates the network to which they belong. The white triangles and yellow triangles are PF and ZF seismological networks maintained by OVPF and Laboratoire Géosciences Réunion (LGSR), respectively. (b) Cross section along A–B is shown at the bottom of the map. The inset on the top right indicates the location of La Réunion island in the Indian Ocean, at the east of Madagascar. Figure modified from an automatic map generated using the WebObs operational system (Beauducel *et al.*, 2020). The color version of this figure is available only in the electronic edition.

insights into the stress regime of volcanic edifices and existing geological structures (e.g., faults, magma plumbing system), which can help us to understand how volcanoes grow, erupt, and collapse (Got *et al.*, 2008; Jay *et al.*, 2011; Lin, 2017; Neal *et al.*, 2019; Matoza, 2020; Wech *et al.*, 2020; Wilding *et al.*, 2023).

La Réunion island hosts two main volcanic edifices: the currently very active Piton de la Fournaise volcano (with 2.5 eruptions per year on average since 2014) and the dormant Piton des Neiges volcano, which has been inactive for 27,000 yr (Famin *et al.*, 2022). Figure 1 shows the seismicity at the scale of the island, in which we can distinguish three main seismogenic areas. First, we can easily identify earthquakes beneath the Piton de la Fournaise volcano that are mainly located within

the volcanic edifice (down to a depth of around 7 km). This seismicity is relatively well studied and clearly associated with the activity of the volcano (Sapin *et al.*, 1996; Collombet *et al.*, 2003; Battaglia *et al.*, 2005; Peltier *et al.*, 2009; Lengliné *et al.*, 2016; Duputel *et al.*, 2019). Seismicity is also recorded in a wide area below the oceanic crust between Piton des Neiges and Piton de la Fournaise. This deep activity is often interpreted as a marker of magma transfer from the deepest part of the plumbing system (Michon *et al.*, 2015; Boudoire *et al.*, 2017). Finally, a sustained seismicity is observed beneath the northern flank of Piton des Neiges volcano, south of Saint-Denis (the capital city of La Réunion). This area is particularly active because it hosts the majority of earthquakes in La Réunion when no VT swarm is recorded at Piton de la Fournaise (Duputel *et al.*, 2021). Moreover, most locally felt earthquakes occur in this region. The origin of this persistent seismic activity is currently unknown and multiple hypotheses have been suggested. Michon *et al.* (2015) proposed that earthquakes in the area could result from extensional stress field maintaining the lithosphere close to failure, suggesting a tectonic origin. Alternatively, the presence of fumarolic sulfur deposits suggests that seismic activity could be associated with an intrusive complex beneath Piton des Neiges volcano (Bénard, 2020). Another possibility is that these earthquakes are caused by the load exerted by the volcanic edifice of Piton des Neiges, as proposed for example in Hawaii (Got *et al.*, 2008). Our understanding of this seismic activity is currently limited by the sparse data coverage in the northern part of the island, resulting in poorly constrained earthquake locations and focal mechanisms.

The aim of this study is to enhance our understanding of the seismic activity beneath Piton des Neiges by leveraging the improved seismological network in the region since 2013. We first present the seismological data available in the region. We then focus on obtaining a high-resolution seismicity catalog using template matching and double-difference earthquake relocation. Finally, after presenting our results, we discuss the origin and time evolution of seismicity at Piton des Neiges volcano.

DATA

Following the creation of the Observatoire Volcanologique du Piton de la Fournaise (OVPF) in 1979, seismological instruments were initially deployed around Piton de la Fournaise to monitor its volcanic activity. At the time, Piton des Neiges was not monitored due to its inactivity and technical limitations concerning data telemetry. A first analog short-period station was installed in the vicinity of Piton des Neiges in 1998 (RMR; see Fig. 2). The network was later extended with three broadband stations in 2012–2013 (PRO, MVL, and CIL). From 2016 onward, the coverage was significantly improved in the northern part of the island with the installation of additional permanent stations and the deployment of temporary stations by the Laboratoire Géosciences Réunion of the University of La Réunion in the framework of the ZF experiment (Fontaine, Barruol, and

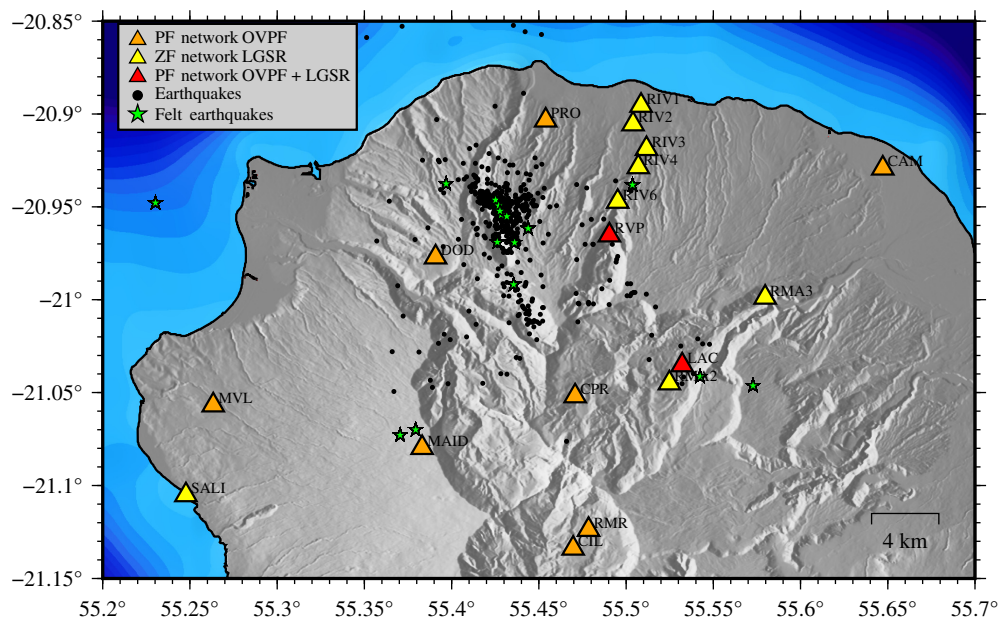


Figure 2. Seismicity and seismological network in the north of La Réunion island. The triangles indicate the location of seismic stations and are color coded by the network (orange for the OVPF PF network, yellow for the LGSR ZF network, and red for stations jointly installed by LGSR and OVPF). All channels are sampled at 100 Hz. The black points represent the events that form the OVPF catalog in the north of the island between January 2013 and September 2022. The green stars show earthquakes felt by the population during the same period. The color version of this figure is available only in the electronic edition.

Gonzalez, 2015; Fig. 2). Such a densification of the seismological network is obviously a good opportunity to study the seismicity of the region.

With the expansion of the seismic network in the north of La Réunion island in 2013, OVPF staff started to identify earthquakes around Piton des Neiges volcano. These earthquakes were localized from manually picked P - and S -wave arrivals using NonLinLoc (Lomax *et al.*, 2001) assuming a 3D model following the topography and a constant $V_P/V_S = 1.7$. In this model, the P -wave velocity is 3.3 km/s at the free surface and increases with depth following a gradient of 0.3 s^{-1} . The same velocity model is used for earthquake localization at the Piton de la Fournaise volcano. In total, nearly 600 seismic events were localized in the vicinity of Piton des Neiges volcano between 2013 and 2022. As shown in Figure 2, these earthquakes are mostly clustered in the northern flank of Piton des Neiges volcano. In this region, the hypocentral locations are scattered over a relatively wide range of depths between 5 and 20 km below sea level (Fig. 1).

IMPROVING THE SEISMICITY CATALOG

Template matching

We used a template matching approach to improve the seismicity catalog in the vicinity of the northern flank of Piton des Neiges volcano. This analysis, which began in January 2013 when the number of available seismic stations was sufficient to obtain good-quality detections, ended in September 2022. The approach relies on template waveforms of manually located earthquakes

shown in Figure 2. Because several earthquakes observed in the study region have very similar waveforms we gathered earthquakes into clusters according to their waveform similarity. For this purpose, we computed correlation coefficients between all earthquake pairs using a 10.24 s time window starting 1 s before the P -wave arrival. The correlation coefficient was averaged for all available stations among PRO, CPR, DOD, RVP, CIL, and MVL over at least three channels. If fewer than three channels were available, the correlation coefficient was set to 0. Using a hierarchical clustering performed with a median linkage, we then gathered earthquakes into clusters with a minimum correlation coefficient of 0.75. We defined one template for each cluster by stacking for each station and each component the corresponding waveforms aligned on the P -wave arrival time. We finally obtained 26 templates. This approach enhances the signal-to-noise ratio of template waveforms and reduces the computational workload of template matching detection. Although stacking multiple waveforms may induce some loss of information by eliminating differences between events associated with different locations or mechanisms, such loss appears minimal given the waveform similarities. As shown by Barrett and Beroza (2014), we find that templates formed by such a stack are very close to the first singular vector obtained after singular value decomposition of the clustered waveforms (Fig. 3). As illustrated in Figure S1, available in the supplemental material to this article, the first singular vector, associated with the highest singular value, contains the most significant common information for all events within each cluster (Harris, 2006).

Once the templates had been defined, we scanned continuous data streams and computed correlation coefficient between the template waveforms and continuous records. These correlation time series were calculated daily for the first nine channels available from the three-component stations PRO, DOD, CPR, MVL, CIL, RVP, RIV4, and RIV6 (Fig. 2). These eight stations were selected for their data quality and geographical location. Following Lengliné *et al.* (2016) approach, we applied a maximum filter over a duration of $\pm 0.1 \text{ s}$ and shifted the correlation signal by correcting for the P -wave travel-time differences between stations (as template time-windows start 1 s before the P -wave arrival). Then, we computed an average

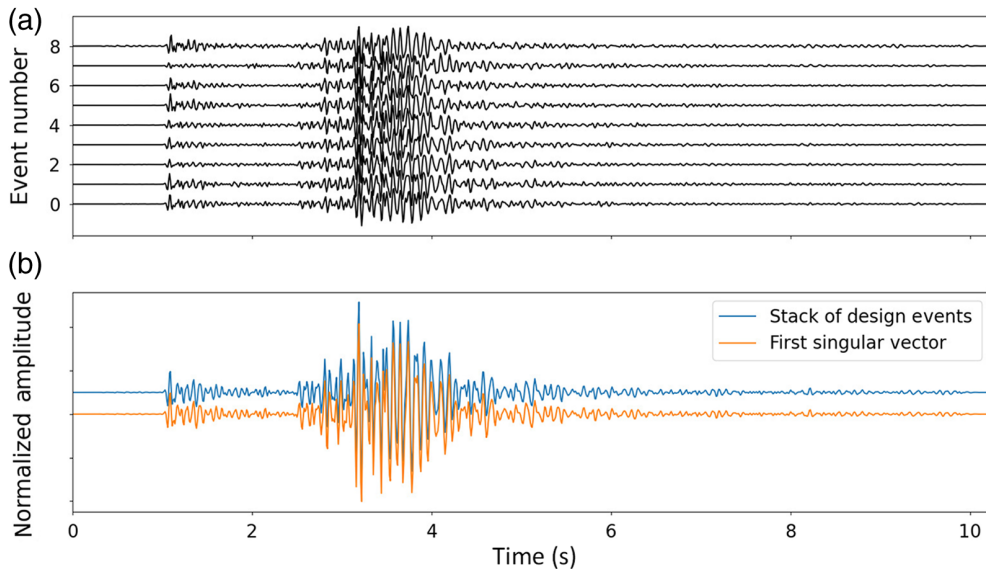


Figure 3. Design of a template waveform from a cluster of similar seismic events. (a) Waveforms at station PRO from a cluster composed of nine earthquakes. (b) The comparison between (blue) the waveform stack and (orange) the first singular vector of the waveforms shown above. Waveforms are aligned on *P*-wave arrival and filtered between 8 and 32 Hz with a fourth-order Butterworth filter. For clarity, the waveforms were normalized by their maximum amplitude. The color version of this figure is available only in the electronic edition.

correlation coefficient after stacking the shifted correlation coefficient of the nine selected channels. Finally, following Lengliné *et al.* (2021), we defined a daily correlation threshold at which this average coefficient indicates an objective detection with a probability of false detection (10^{-5} per day and per template). To be considered as separate events, two detections must be separated by at least 10 s.

Using this approach, we detected 18,178 events between January 2013 and September 2022, which is over 30 times larger than the size of our initial manual catalog. The waveforms of these detections are represented chronologically for the vertical component of station PRO in Figure 4. In this Figure, we can clearly identify the *P*-wave arrival at ~ 1 s (i.e., 100 samples) followed by an *S*-wave arrival around 2.6 s for a large number of events. Although some events seem to be associated with a different *P*–*S* travel-time delay, this similarity suggests that a large portion of the detected events are clustered in a relatively small area of the studied region.

Magnitude estimates

To calculate a local magnitude, we followed the procedure described by Richter (1935) and the corrections noted by Hutton and Boore (1987) so that an M_L 3.0 earthquake has a 10 mm amplitude at a 17 km hypocentral distance on a Wood–Anderson instrument,

$$\log_{10}(A) + 2.0 = M_L + \alpha \log_{10}\left(\frac{R}{17}\right) + K(R - 17), \quad (1)$$

in which A is the half of peak-to-peak Wood–Anderson amplitude; M_L is the local magnitude; α is the geometric spreading factor; R is the hypocentral distance in kilometers; and K is the attenuation factor. To determine A , we corrected the recorded waveforms from their instrumental response and convolved them with a Wood–Anderson response. We then used a 4 s window starting 1 s before the *S* wave to calculate A . Using these amplitude values for the horizontal components of all PF stations, we calculated the value of M_L for earthquakes in the initial OVPF catalog by inverting equation (1) for the local magnitudes M_L and the attenuation coefficient K (we found $K \approx -0.012$).

Figure S2 shows the difference between local magnitudes M_L and duration magnitudes M_d previously estimated at OVPF. The comparison shows an average offset of +0.7 magnitude unit between M_L and M_d . The larger values of M_L likely result from the fact that our M_d estimates are not properly calibrated for deep earthquakes below Piton des Neiges. Duration magnitudes in La Réunion have been calibrated for shallow VT earthquakes at Piton de la Fournaise that are usually associated with long coda tails in seismograms. Apart from this constant offset, there is globally a good agreement between M_L and M_d , with a standard deviation of 0.4 magnitude units.

For each template matching detection, we then selected the event from the initial OVPF catalog waveforms that best correlate with the waveforms of the detected event (considering the average correlation coefficient among PF stations). The local magnitude of the detected event (M_L^d) was then calculated at each PF station using

$$M_L^d = M_L^c + \log_{10} \frac{A^d}{A^c}, \quad (2)$$

in which $M_L^{c,d}$ and $A^{c,d}$ are respectively the local magnitude and horizontal amplitude of the cataloged and detected events. M_L was finally estimated using the average of M_L^d computed at each station.

Figure 5 shows the magnitude distributions of the initial OVPF catalog and of the template matching detections. It clearly highlights the improvement of the catalog's completeness: by increasing the number of detected events by a factor of ~ 30 , template matching also lowers the magnitude of completeness from $M_c \approx 1.8$ in the initial catalog to $M_c \approx 0.8$.

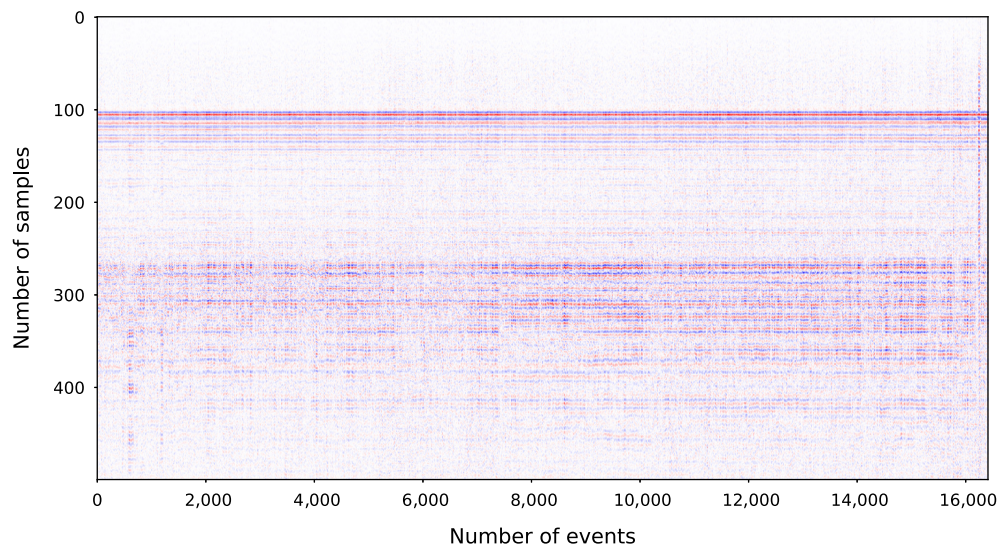


Figure 4. Template matching detections sorted chronologically. Waveforms are shown for the vertical component of station PRO. They are aligned on the *P*-wave arrival, normalized, and filtered between 8 and 32 Hz with a fourth-order Butterworth filter. The color version of this figure is available only in the electronic edition.

Earthquake relocation

We relocated earthquakes using the GrowClust3D algorithm (Trugman *et al.*, 2023), the particularity for which is to combine hierarchical clustering and double-difference relocation of seismic events in a 3D Earth model. The method is based on an L1-norm objective function that is less sensitive to outliers and allows the processing of large-scale relocation problems possibly containing multiple seismicity clusters.

To perform the relative relocation, we used differential travel times of pairs of events observed at common stations. These differential travel times were estimated by cross-correlating waveform pairs using respectively 1 and 3 s windows around the *P*- and *S*-wave arrivals. We used vertical components to estimate *P*-wave travel-time delays and horizontal

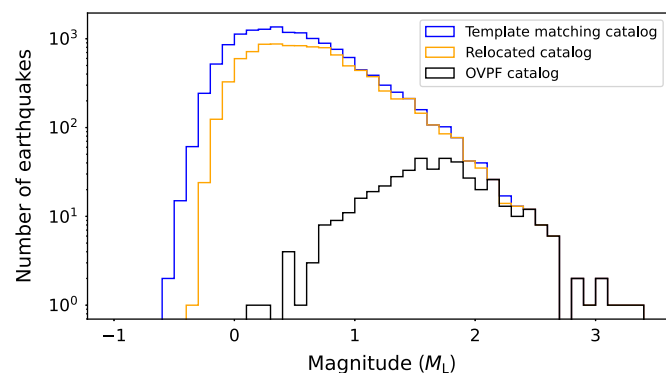


Figure 5. Magnitude distributions for (black) the OVPF catalog, (blue) the template matching catalog, and (orange) the relocated catalog (compare with the Earthquake relocation section). The color version of this figure is available only in the electronic edition.

components for *S*-wave travel-time delays (we only kept the horizontal component with the best correlation). To ensure the quality of our measurements, we considered a minimum correlation threshold of 0.5, which resulted in 7,705,128 differential travel times (taking into account *S*- and *P*-wave arrivals). Relocation was conducted using the same 3D velocity model as the one used for NonLinLoc earthquake locations of the OVPF catalog (i.e., a velocity gradient following the topography). In GrowClust3D, we set the maximum distance allowed to join two events in a same cluster to 2 km and the maximum distance allowed to join two clusters to 1 km. Using such criteria, 12,082 events out of the 18,178 detected events were relocated. We applied an additional quality-screening criterion by only considering relocations with a minimum of 10 event pairs, resulting in a catalog of 10,086 relocated events. To obtain uncertainty estimates, we also used a bootstrap approach in which GrowClust3D is repeating the relocation process for 100 random resampling of the original data set (Trugman *et al.*, 2023).

The resulting relocated event catalog and associated uncertainty is shown in Figure 6. The seismicity is clustered into four discrete clusters of more than 100 events that are mainly distributed under the northern flank of Piton des Neiges. The largest of these clusters includes 9673 events. As illustrated in A–B profiles shown in Figure 6b,d, this main cluster delineates a well-defined planar structure that is strongly dipping to the northeast (strike angle: 302°, dip angle: 43°). The depth of this planar structure ranges from 9 to 10 km below sea level. According to previous estimates of the oceanic crust depth (Gallart *et al.*, 1999; Fontaine, Barruol, Tkalcic, *et al.*, 2015), the observed planar structure would therefore be located in the oceanic crust under the volcanic edifice of Piton des Neiges. The secondary clusters exhibit a similar orientation, suggesting the potential presence of multiple similarly aligned structures within the oceanic crust (see Fig. 6c).

Focal mechanisms

To estimate focal mechanisms, we extracted *P*-wave polarities from the OVPF catalog. We then computed azimuth and take-off angles for each station, considering earthquake locations in the relocated catalog and using the 3D velocity model

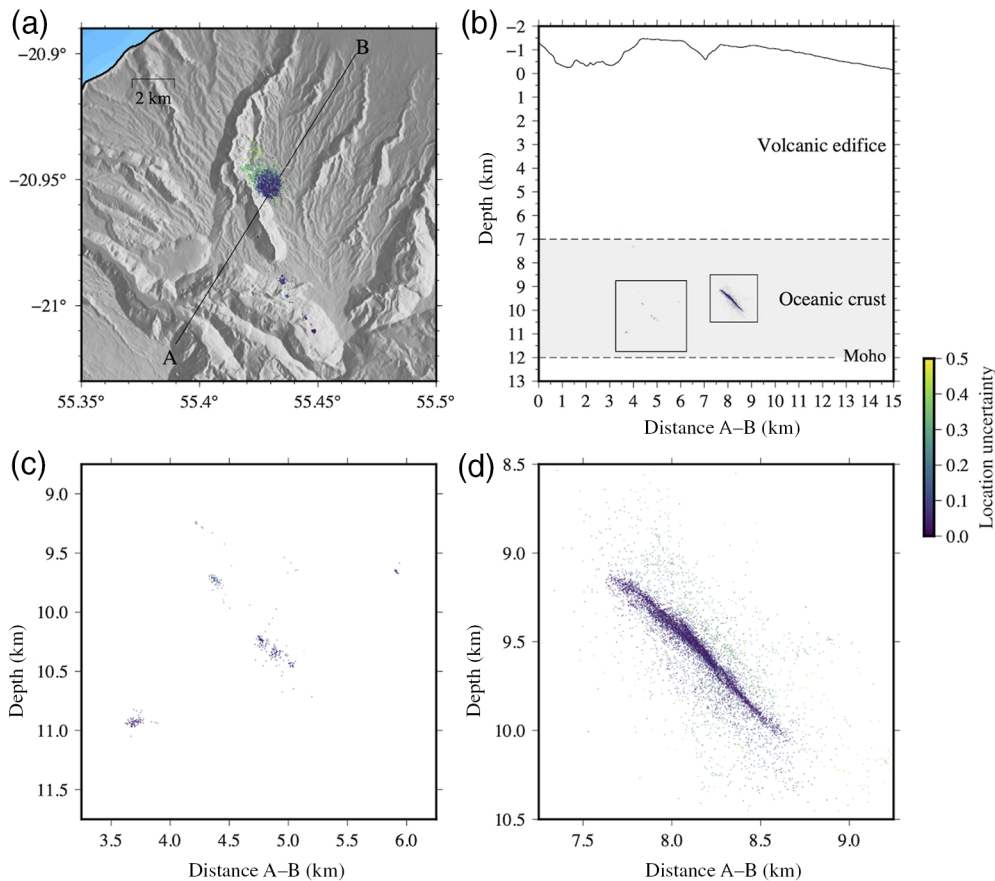


Figure 6. Relocated earthquake catalog. (a) Map view of the relocated catalog. A–B indicate the orientation of the cross section shown in panels (b–d). (b) Relocated events projected along profiles A–B. Depth of the oceanic crust is taken from Gallart *et al.* (1999) and Fontaine, Barroul, Tkalcic, *et al.* (2015). (c) Zoom on secondary clusters. (d) Zoom on the largest cluster. Colors indicate the location uncertainty (in km). The main cluster defines a planar structure that is strongly dipping to the northeast (best-fitting plane gives a strike angle of 302° and a dip angle of 43°). The color version of this figure is available only in the electronic edition.

described above (compare with the [Data](#) and [Earthquake relocation](#) sections). Finally, we used the HASH algorithm (Hardebeck and Shearer, 2002) to find focal mechanisms that best match our first-motion observations (compare with supplemental text S1). To ensure quality of the results, we consider mechanisms corresponding to classes A and B defined by Hardebeck and Shearer (2002, average misfit ≤ 0.20 , root mean square fault plane uncertainty $\leq 35^\circ$, station distribution ratio ≥ 0.4 and mechanism probability ≥ 0.6). Examples of focal mechanism determination from *P*-wave polarities are presented in Figure S3.

Most of the resulting focal mechanisms shown in Figure 7 and Figure S4 indicate reverse fault motion. These mechanisms align well with the orientation of the main planar structure presented in Figure 6d. Reverse mechanisms are also consistent with the overall alignment of secondary clusters, as depicted in Figure 6b,c. These findings thus suggest that the majority of earthquakes in the north of La Réunion island are linked to the activity of reverse faults located in the oceanic crust beneath the Piton des Neiges volcanic edifice.

Time evolution of the seismicity

Although the gradual densification of the seismic network presents an opportunity for our study, the improvement of the observational network also influences the number of recorded earthquakes. Figure 8 clearly illustrates that the deployment of the ZF network in the study region leads to a larger number of detected earthquakes. When the network coverage is sparser (e.g., before 2016), the detection of smaller events becomes challenging, resulting in catalog completeness at higher magnitudes. Between 2016 and 2021, the network remained relatively stable, which mitigates spurious variations caused by station coverage variability. As shown in Figure 9a, the time periods from 2016 to 2018 and from 2019 to 2021 depict very similar magnitudes of completeness ($M_c = 0.8$), suggesting minimal impact of the seismic network on the detection level for these two periods. However, there is a

noticeable data gap from November 2018 to April 2019. This gap is due to the failure of two stations (PRO and RVP), which are in close proximity to the main seismicity cluster.

After extracting earthquakes above a magnitude of completeness $M_c = 0.8$, we then evaluated the temporal variation in seismicity rate between 2016 and 2021. Results in Figure 9b do not show very strong peaks of seismic activity as observed during magma intrusions on active volcanoes (McNutt, 1996; Traversa and Grasso, 2010) or during mainshock–aftershock sequences (Zhuang *et al.*, 2012). The coefficient of variation of interevent time delays (C_v , defined as the ratio of the variance to the mean interoccurrence time) is close to 1 (i.e., $C_v \sim 1.2$), which is consistent with what is expected from a stationary Poisson process without any strong temporal clustering or periodicity in the seismicity (Kagan and Jackson, 1991). There is a noticeable increase in activity starting in April 2018 with no obvious mainshock event (see Fig. S5). This swarmlike activity is characterized by an increase of the seismicity rate from 1.0 to 2.4 event/day. After this rapid increase in activity, the seismicity rate slowly decreases to reach the background level in 2020.

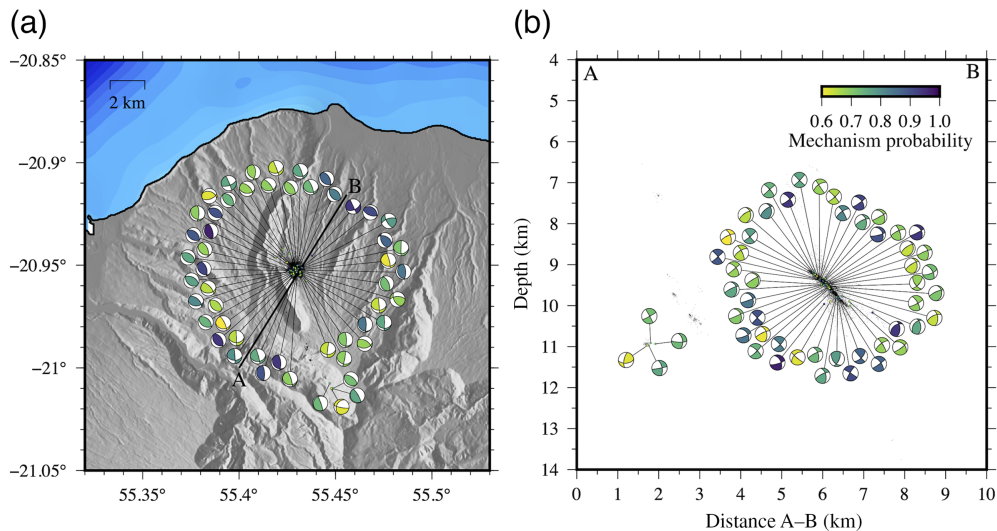


Figure 7. Focal mechanisms of relocated earthquakes. (a) Map view of the focal mechanisms and relocated catalog (in black). (b) Focal mechanisms and relocated catalog projected along profiles A–B. Colors indicate the mechanism probability as defined by Hardebeck and Shearer (2002). Only focal mechanisms with an average misfit ≤ 0.20 , a root mean square fault plane uncertainty $\leq 35^\circ$, a station distribution ratio ≥ 0.4 and a mechanism probability ≥ 0.6 are represented. These criteria correspond to quality classes A and B in Hardebeck and Shearer (2002). Most of the mechanisms show reverse-fault mechanisms the orientation for which is consistent with the planar structure shown in Figure 6. The color version of this figure is available only in the electronic edition.

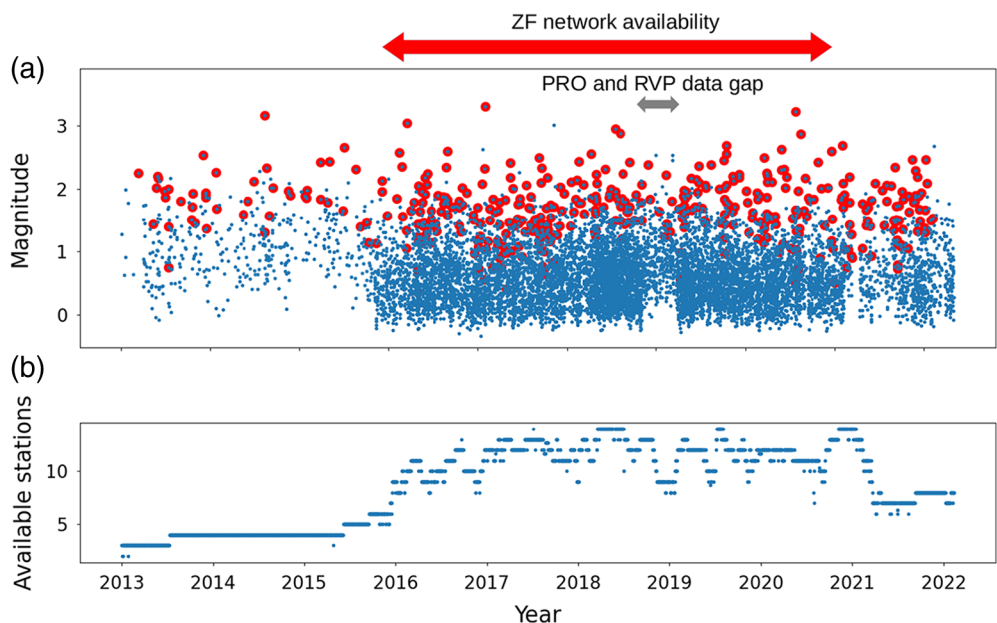


Figure 8. Relocated earthquake catalog from 2013 to 2022. (a) Earthquake magnitudes as a function of time are shown. (b) The number of available stations in the study area. The red circles represent events already present in the OVPF catalog, and blue circles denote new detections. A red arrow indicates the time period of ZF network data availability, and a gray arrow outlines the data gap from November 2018 to April 2019 when station PRO and RVP were not operating. The color version of this figure is available only in the electronic edition.

DISCUSSION

Although our analysis primarily covers the 2013–2021 time period, one might wonder whether the main seismicity cluster was already active prior to this period. To analyze its long-term activity, we performed template matching using vertical short-period recordings from RMR, the only station available in the north of La Réunion island from 1999 to 2014. We used OVPF events located on the main fault and recorded by RMR between 2013 and 2014 as templates for our detections between 1999 and 2014. From 2013 to 2021, we repeated the experiment using the vertical component of the broadband station CIL, installed near RMR in 2013. The results presented in Figure 10 indicate that the fault has been active at least since 1999. On average, the seismicity rate was smaller from 1999 to 2012 (0.3 event/day) than from 2013 to 2021 (0.6 event/day). This discrepancy is likely due to the difference in data quality between stations RMR and CIL: RMR was equipped with a short-period sensor (Mark Product LAC 1 Hz with Radio FM telemetry) and is subject to numerous data gaps, whereas CIL uses a broadband sensor (Güralp CMG-3ESPC retrieved through internet connection). However, it is worth noting a substantial increase in seismicity rate from May 2011 to March 2013, similar to the increase observed from April 2018 to November 2018 (also visible in Fig. 9b).

One may question whether the increased seismic activity observed in 2011 and 2018 could be associated with deep magma activity beneath the

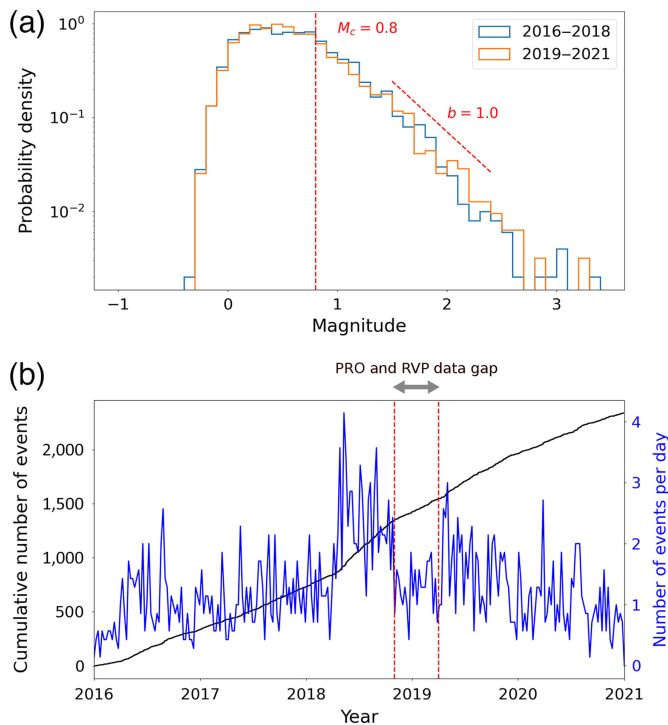


Figure 9. Seismic activity between 2016 and 2021. (a) Magnitude distributions before (blue) and after (orange) the data gap from November 2018 to April 2019 during which near-field stations PRO and RVP were unavailable (compare with Fig. 8). b -values are estimated for the two time periods using $b = \log_{10}(e)/(\bar{m} - M_c)$, in which \bar{m} is the mean magnitude and M_c is the magnitude of completeness (Aki, 1965). (b) Seismic activity from 2016 to 2021. We show the cumulative number of events (in black) and the daily seismicity rate (in blue). Seismicity rate is averaged in a 7 day time window. We only consider events with magnitudes greater than the magnitude of completeness $M_c = 0.8$ as shown in panel (a). We notice a significant increase in seismicity rate from April 2018 to November 2018. The color version of this figure is available only in the electronic edition.

Piton des Neiges. Seismic activity linked to residual magma processes under dormant volcanoes has been documented in previous studies (Lin, 2017; Wech *et al.*, 2020). In the study area, fumarolic sulfur deposits have been observed at the surface (Lopoukhine and Stieltjes, 1978; Rançon and Rocher, 1985). However, the nature of these deposits remains unclear: they could be fossil condensates deposited by former degassing or a current degassing process associated with magma activity beneath Piton des Neiges. In the latter case, the observed seismic activity might be linked to deep volcanic activity. It is generally accepted that the magma currently feeding Piton de la Fournaise originates from a zone of magmatic underplating below the oceanic crust between Piton des Neiges and Piton de la Fournaise (Michon *et al.*, 2016; Boudoire *et al.*, 2017; Duputel *et al.*, 2021). If magma still exists beneath the Piton des Neiges, it may share the same origin. In such a scenario, one might expect to observe a correlation between long-term seismic activity at Piton des Neiges and the activity at Piton de la Fournaise. However, as shown in Figure S6, no clear

correlation exists between seismic activity at Piton des Neiges and the timing of eruptions at Piton de la Fournaise. This lack of correlation may result from the fact that eruption history largely depends on the shallow stress state of the Piton de la Fournaise edifice (Got *et al.*, 2013) and is not a direct indicator of deep magma feeding processes. More suitable indicators for tracking deep magma inputs include changes in distal GNSS baselines and deep seismicity between Piton des Neiges and Piton de la Fournaise (Battaglia *et al.*, 2005; Lengliné *et al.*, 2016; Peltier *et al.*, 2016). The results shown in Figures S7 and S8 do not reveal any clear relationship between deep magma activity at Piton de la Fournaise and Piton des Neiges volcanoes. It is worth noting that variations in seismic activity at Piton des Neiges are considerably smaller than those observed at Piton de la Fournaise. At Piton de la Fournaise, the seismicity rate typically undergoes significant fluctuations, ranging from a few events per day during inter-eruptive periods to several hundreds of earthquakes per hour during magma intrusions (Duputel *et al.*, 2019). In addition, there are no pronounced variations in b -values over the studied time period (compare with Fig. 9a), in contrast to what is often observed during magma intrusions (Jacobs and McNutt, 2010; Traversa and Grasso, 2010). Therefore, although it cannot be definitely ruled out, there is no strong evidence to support a direct link between seismic activity at Piton des Neiges and a transient magmatic process. Moreover, there is no clear correlation with precipitation in the region (compare with Fig. S9), which does not support any rainfall-triggered earthquake activity as reported, for example, by Hainzl *et al.* (2006).

It is important to note that most fluctuations in seismic activity at Piton des Neiges are confined to the main reverse fault plane identified in the present study. As shown in Figure S10, other regions north of La Réunion island do not exhibit similar variations in seismicity rate. The occurrence of earthquake swarms on faults is often associated with transient aseismic slip in various volcanic or tectonic contexts (Segall *et al.*, 2006; Lohman and McGuire, 2007; Vallée *et al.*, 2013; Gualandi *et al.*, 2017). To investigate whether our observations align with this scenario, we searched for repeating earthquakes, which are often regarded as markers of aseismic fault slip. These repeating earthquakes result from the repeated failure of embedded asperities on a slowly creeping fault and are characterized by similar source location and waveforms (Nadeau and Johnson, 1998; Lengliné and Marsan, 2009; Uchida, 2019). To search for such repeating events, we identify earthquake families exhibiting very similar waveforms and associated with overlapping ruptures. Further details of the selection process are provided in text S2 of the online supplementary. Using this approach, we detected a total of 795 repeating earthquakes from 2016 to 2021. These repeating earthquakes are spatially distributed all along the entire fault plane (Fig. 11a,b). Although repeating earthquakes occurred through the entire time period, they were temporally clustered

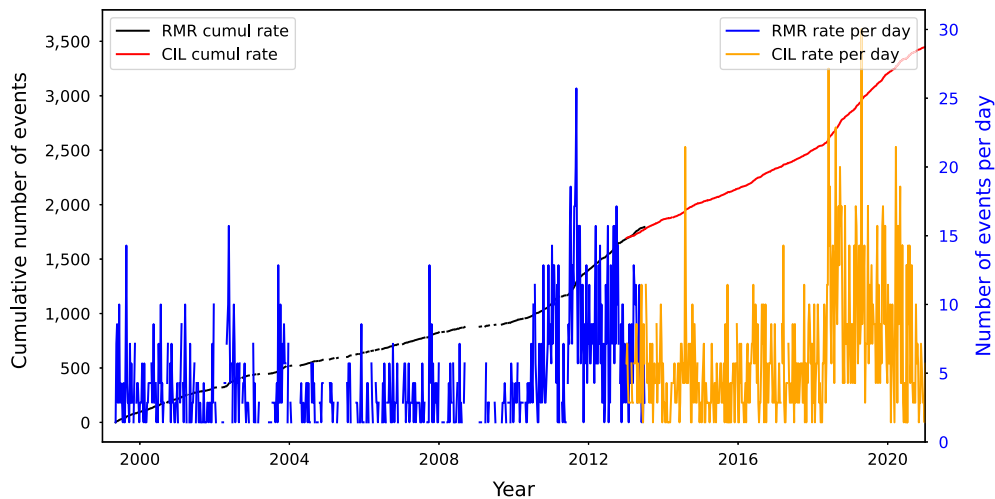


Figure 10. Seismic activity from 1999 to 2022 estimated from single station template matching. We show the cumulative number of events obtained using station RMR (black line) and station CIL (red line). We also present the daily earthquake count detected using RMR (blue line) and CIL (orange line). We use a 7 day window averaging to estimate the daily seismicity rate. The blank spaces in seismicity rate and cumulated seismicity curves represent periods of missing data. We notice a significant increase in seismicity rate from May 2011 to March 2013 similar to the one observed from April 2018 to November 2018. The color version of this figure is available only in the electronic edition.

between April 2018 and November 2018, coinciding with the seismic swarm observed in our catalog (Fig. 11c). With this repeater catalog, we then estimated the time evolution of aseismic slip on the fault (Fig. 11d). This estimate followed the approach of Kato *et al.* (2012), using a circular crack model with a constant stress drop of 3 MPa to evaluate the individual repeater slip amplitudes. The contributions of individual repeaters are then summed over time and averaged by the number of repeater families to estimate cumulative slip evolution. The results presented in Figure 11d suggest that the onset of the seismic swarm in April 2018 was marked by an increase in the fault-slip rate, which subsequently decreased gradually until the beginning of 2020.

In addition to the observed variations in seismicity rates, it is interesting to highlight that a significant number of earthquakes in the northern part of La Réunion island are associated with reverse faulting, even outside of the primary seismic cluster. As illustrated in Figure S11, the majority of focal mechanisms exhibit orientations similar to the fault under the north flank of Piton des Neiges. This prevalence of reverse faulting suggests a predominantly compressive stress regime in the northern sector of the island. This finding contradicts the interpretation put forth by Michon *et al.* (2015), which suggested that seismic activity in this area resulted from a regional extensional stress field caused by opposing forces (edifice loading versus thermal erosion of the lithosphere). The origin of this compressive stress field could be attributed to the flexural deformation of the lithosphere induced by the load imposed by the Piton des Neiges edifice. Flexural deformation of the lithosphere has previously

been invoked to explain deep-seated seismicity beneath volcanic edifices in Hawaii (Ten Brink and Brocher, 1987; Watts and Ten Brink, 1989; Wessel, 1993; Got *et al.*, 2008). However, in contrast to the Hawaiian hotspot, no observable lithospheric flexure has been documented beneath La Réunion island (Gallart *et al.*, 1999). To address this absence of lithospheric deformation, it has been postulated that the load caused by the volcanic edifice is counterbalanced by the upward force exerted by the plume (Bonneville *et al.*, 1997; Lénat *et al.*, 2009). In this scenario, a compressive stress regime can arise just below the volcanic edifice due to the combined effect of edifice loading and plume upwelling as

depicted in figure 9b of Gerbault *et al.* (2017, for depth = 0 km and $X = -160$ km).

Another important consideration in understanding seismicity in the context of edifice loading relates to the orientation of focal mechanisms. If earthquakes were solely a consequence of Piton des Neiges' gravitational load, one might expect to observe focal mechanisms oriented radially around the edifice, with the strike-angle dependent on the azimuth relative to the summit. However, this radial orientation is not evident in Figure S11. Instead, a significant portion of focal mechanisms displays a strike angle of about N300°, resembling the reverse fault geometry depicted in Figure 6. This intriguing alignment corresponds to the distribution of numerous cinder cones between Piton des Neiges and Piton de la Fournaise, which have been interpreted as indicators of a preferential magma intrusion path along the N120° azimuth (Chevalier and Bachèlery, 1981; Villeneuve and Bachèlery, 2006; Michon *et al.*, 2015). This alignment suggests the presence of pre-existing structural weaknesses in the region, which could play a pivotal role in the orientation of both focal mechanisms and magma propagation. This N120° alignment might possibly correspond to normal faults in the oceanic crust, originally formed at the Mid-Indian Ridge in which the spreading axis also aligns at N120° (Michon *et al.*, 2007; Chaput *et al.*, 2017). These pre-existing faults could be reactivated as reverse faults due to the edifice load and the regional stress field. Furthermore, these faults may serve as preferential pathways for magma transport between Piton des Neiges and Piton de la Fournaise volcanoes. Hydrothermal activity may also contribute to the reactivation of these reverse faults. Piton des Neiges

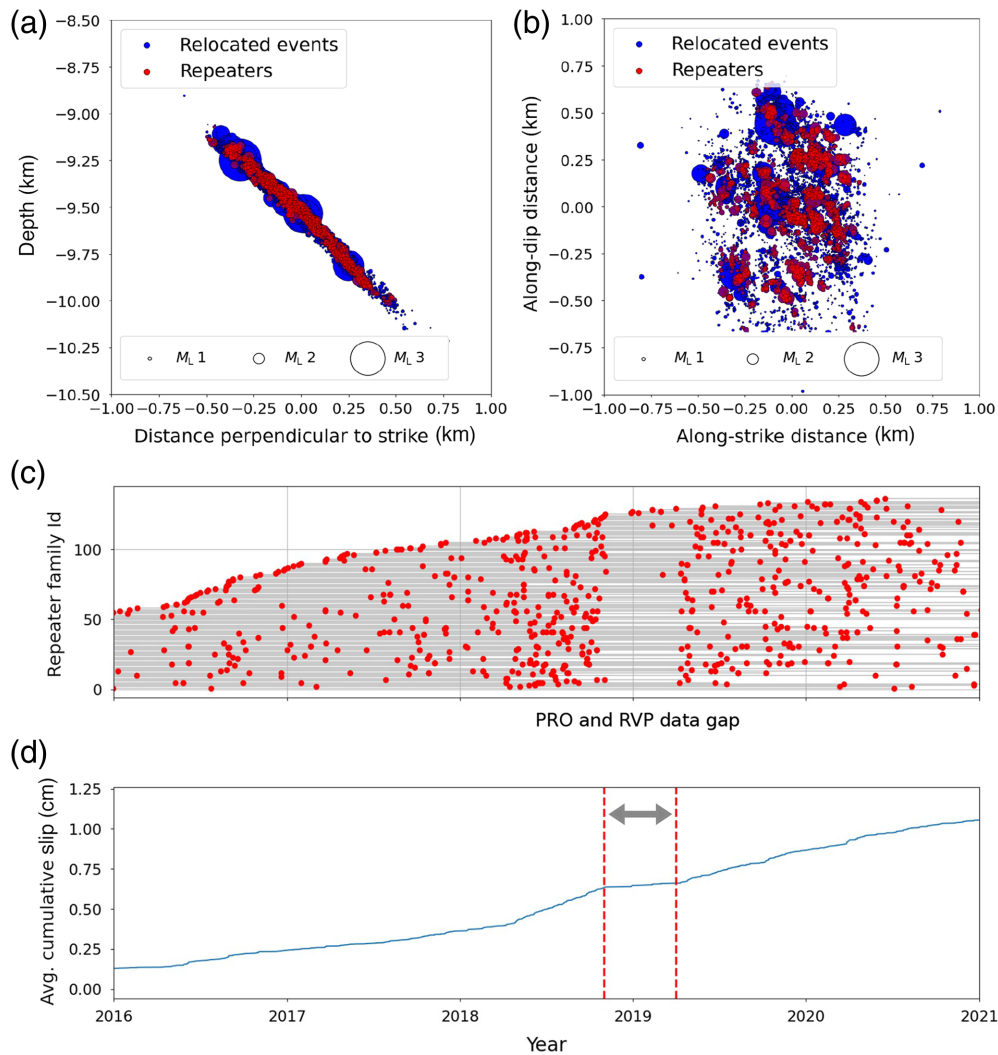


Figure 11. Repeating earthquake activity. (a) Cross section and (b) on-fault projection of relocated earthquakes from 2016 and 2021. Repeaters are shown in red, and other earthquakes are shown in blue. The size of the dots indicates the relative magnitudes of the events. Repeaters are spatially distributed all along the fault. (c) Repeater families sorted chronologically (“Id” indicates the identification number of the repeater family). (d) Cumulative slip estimated from the repeater activity. Slip is averaged over the number of repeater families. The color version of this figure is available only in the electronic edition.

volcano exhibits signs of hydrothermal activity, including thermal springs, fumarole deposits, and CO_2 anomalies (Rançon, 1985; Marty *et al.*, 1993; Bénard *et al.*, 2023). This hydrothermal activity could cause fluid overpressure, potentially leading to the reactivation of a normal fault into a reverse fault (Sibson, 2014).

The seismic activity of the fault we have identified in the oceanic crust beneath Piton des Neiges volcano is a prominent feature in the seismicity of La Réunion island. On average, from 2016 to 2021, this fault experienced an average of 1.3 earthquakes per day, each with a magnitude $M \geq 0.8$. This makes it the most active region of La Réunion aside from magma intrusions at Piton de la Fournaise volcano (Duputel *et al.*, 2021). Considering the dimensions of the structure derived from our catalog, this fault could produce a magnitude ~ 4.2 earthquake

if ruptured in a single event, assuming a stress drop of 3 MPa on a 1×1.5 km rectangular fault (Parsons *et al.*, 1988). Such an event would be widely felt on the island and could cause minor damage to buildings and other infrastructures. Given a b -value of 1, the likelihood of observing such a significant earthquake in the next 5 yr stands at $\sim 61\%$ (see text S3). However, it is important to note that this estimate does account for the possibility of the fault being partially unloaded due to the occurrence of slow-slip events, as suggested by the swarmlike activities observed in 2011 and 2018.

CONCLUSION

By employing a template matching approach, we detected 18,178 earthquakes representing 8 yr of seismicity at Piton des Neiges volcano from 2013 to 2021. Using double-difference relocation, we relocated 10,086 events representing 55.48% of our template matching catalog. The application of relative relocation significantly sharpened the seismicity in the area, revealing a primary northeastward dipping structure under the north flank of Piton des Neiges. Results also indicate smaller secondary seismicity

clusters with a similar orientation. The determination of focal mechanisms indicates fault orientations that are consistent with these structures, revealing active reverse faults located within the oceanic crust beneath the volcanic edifice.

Although our study has significantly improved the characterization of seismic activity on La Réunion island, the origin of the sustained activity beneath the north flank of Piton des Neiges remains puzzling. Our results show that this area has experienced continuous seismicity since 1999, with two periods of increased seismic activity in 2011 and 2018. These increases of seismicity rate do not correlate with markers of deep magma activity and are confined to the primary reverse fault identified under the north flank of Piton des Neiges. Repeater analysis suggest that such seismicity fluctuations

could be caused by small variations in the fault creep rate (compare with Fig. 11d). The lack of a clear link to deep magmatic activity, combined with the consistent orientation of fault mechanisms in the north of the island, suggests that earthquakes occur on pre-existing faults that are primarily loaded by tectonic stresses and the weight of the edifice. Although seismic activity does not seem to be directly tied to deep magmatism, we cannot rule out a potential reactivation of Piton des Neiges. Recent instances such as Cumbre Vieja (Gottsmann *et al.*, 2006; Romero *et al.*, 2022, La Palma) or Fani Mahoré (Feuillet *et al.*, 2021, Mayotte) show that dormant volcanoes can reactivate very rapidly.

To gain deeper insights, a more precise imaging of the structure beneath Piton des Neiges seems imperative. Currently, our understanding of the internal structure of La Réunion relies on 1D and 2D images obtained from receiver functions and a northeast–southwest seismic transect between Piton des Neiges and Piton de la Fournaise (Gallart *et al.*, 1999; Fontaine, Barruol, Tkalcic, *et al.*, 2015). Regional 3D tomography could provide more detailed structural information, as demonstrated, for example, by Got *et al.* (2008) in Hawaii island. These images, in particular, could help pinpoint residual magmatic storage zones below Piton des Neiges and further investigate any possible link with the seismicity.

DATA AND RESOURCES

The data used in this study were acquired by the Volcanological Observatory of Piton de la Fournaise (OVPF-IPGP) and are accessible via the VOLOBSIS Portal at <http://volobsis.ipgp.fr>. Validated data can be accessed through the RESIF data portal <http://resif.fr>. Data from the “Rivière des Pluies” network doi: [10.15778/RESIF.ZF2015](https://doi.org/10.15778/RESIF.ZF2015) are available under the ZF experiment code (Fontaine, Barruol, and Gonzalez, 2015). The supplemental material includes technical details on the methods used, such as the calculation of focal mechanisms and repeaters. They also include figures in support of the methods described, and the discussion.

DECLARATION OF COMPETING INTERESTS

The authors acknowledge that there are no conflicts of interest recorded.

ACKNOWLEDGMENTS

The authors thank Bhavani Bénard, Muriel Gerbault, and Aline Peltier for enlightening discussions. The authors are also grateful to Laurent Michon for his helpful reviews and comments. In addition, the authors would like to thank the editor Shengji Wei, and two anonymous reviewers for their valuable feedback, which enabled us to enhance the article. This work was supported by the European Research Council (under the European Union’s Horizon 2020 research and innovation program under Grant Agreement Number 805256).

REFERENCES

Aki, K. (1965). Maximum likelihood estimate of b in the formula $\log N = a - bM$ and its confidence limits, *Earthq. Res. Inst.* **43**, 237–239.

- Barrett, S. A., and G. C. Beroza (2014). An empirical approach to subspace detection, *Seismol. Res. Lett.* **85**, no. 3, 594–600.
- Battaglia, J., V. Ferrazzini, T. Staudacher, K. Aki, and J.-L. Cheminée (2005). Pre-eruptive migration of earthquakes at the Piton de la Fournaise volcano (Réunion Island), *Geophys. J. Int.* **161**, no. 2, 549–558.
- Beauducel, F., D. Lafon, X. Béguin, J.-M. Saurel, A. Bosson, D. Mallarino, P. Boissier, C. Brunet, A. Lemarchand, C. Anténor-Habazac, *et al.* (2020). WebObs: The volcano observatories missing link between research and real-time monitoring, *Front. Earth Sci.* **8**, 48, doi: [10.3389/feart.2020.00048](https://doi.org/10.3389/feart.2020.00048).
- Bénard, B. (2020). Caractérisation du système hydrothermal du Piton des Neiges par des méthodes géochimiques et isotopiques, *Theses*, Université de la Réunion (in French).
- Bénard, B., V. Famin, B. Sanjuan, F. Vimeux, B. Aunay, P. Agrinier, and G. Lebeau (2023). An integrated geochemical spatial and temporal survey of thermal springs to characterize the geothermal resource of a volcano (Piton des Neiges, Réunion Island), *Appl. Geochem.* **154**, 105689, doi: [10.1016/j.apgeochem.2023.105689](https://doi.org/10.1016/j.apgeochem.2023.105689).
- Bonneville, A., R. P. V. Herzen, and F. Lucazeau (1997). Heat flow over Reunion hot spot track: Additional evidence for thermal rejuvenation of oceanic lithosphere, *J. Geophys. Res.* **102**, no. B10, 22,731–22,747.
- Boudoire, G., M. Liuzzo, A. D. Muro, L. M. Valérie Ferrazzini, F. Grassa, A. Derrien, N. Villeneuve, A. Bourdeu, C. Brunet, G. Giudice, *et al.* (2017). Investigating the deepest part of a volcano plumbing system: Evidence for an active magma path below the western flank of Piton de la Fournaise (La Réunion Island), *J. Volcanol. Geotherm. Res.* **341**, 193–207.
- Brenguier, F., D. Clarke, Y. Aoki, N. Shapiro, M. Campillo, and V. Ferrazzini (2011). Monitoring volcanoes using seismic noise correlations, *C.R. Geosci.* **343**, 633–638.
- Chaput, M., V. Famin, and L. Michon (2017). Sheet intrusions and deformation of Piton des Neiges, and their implication for the volcano-tectonics of La Réunion, *Tectonophysics* **717**, 531–546.
- Chevalier, L., and P. Bachèlery (1981). Evolution structurale du volcan actif du Piton de la Fournaise, Ile de La Réunion—océan indien occidental, *Bull. Volcanol.* **44**, 723–741 (in French).
- Chouet, B. (2003). Volcano seismology, *Pure Appl. Geophys.* **160**, no. 3, 739–788.
- Chouet, B., and R. S. Matoza (2013). A multi-decadal view of seismic methods for detecting precursors of magma movement and eruption, *J. Volcanol. Geotherm. Res.* **252**, 108–175.
- Collombet, M., J.-R. Grasso, and V. Ferrazzini (2003). Seismicity rate before eruptions on Piton de la Fournaise volcano: Implications for eruption dynamics, *Geophys. Res. Lett.* **30**, no. 21, 2099, doi: [10.1029/2003GL017494](https://doi.org/10.1029/2003GL017494).
- Duputel, Z., V. Ferrazzini, O. Lengliné, F. R. Fontaine, and F. Massin (2021). Seismicity of La Réunion island, *C.R. Geosci.* **353**, no. S1, 237–255, doi: [10.5802/crgeos.77](https://doi.org/10.5802/crgeos.77) (in French).
- Duputel, Z., O. Lengliné, and V. Ferrazzini (2019). Constraining spatiotemporal characteristics of magma migration at Piton de la Fournaise volcano from pre-eruptive seismicity, *Geophys. Res. Lett.* **46**, no. 1, 119–127.
- Famin, V., C. Paquez, M. Danišik, N. J. Gardiner, L. Michon, C. L. Kirkland, C. Berthod, B. Friedrichs, A. K. Schmitt, and P. Monié (2022). Multitechnique geochronology of intrusive and explosive activity on Piton des Neiges volcano, Réunion island,

- Geochem. Geophys. Geosys.* **23**, no. 5, e2021GC010214, doi: [10.1029/2021gc010214](https://doi.org/10.1029/2021gc010214).
- Feuillet, N., S. Jorry, W. C. Crawford, C. Deplus, I. Thinon, E. Jacques, J.-M. Saurel, A. Lemoine, F. Paquet, C. Satriano, *et al.* (2021). Birth of a large volcanic edifice offshore Mayotte via lithosphere-scale dyke intrusion, *Nature Geosci.* **14**, no. 10, 787–795.
- Fontaine, F. R., G. Barruol, and A. Gonzalez (2015). Rivière des pluies project, La Réunion Island, 2015–2018, doi: [10.15778/resif.zf2015](https://doi.org/10.15778/resif.zf2015).
- Fontaine, F. R., G. Barruol, H. Tkalcic, I. Wolbern, G. Rumpker, T. Bodin, and M. Haugmard (2015). Crustal and uppermost mantle structure variation beneath La Réunion hotspot track, *Geophys. J. Int.* **203**, no. 1, 107–126.
- Frank, W., N. Shapiro, and A. Gusev (2018). Progressive reactivation of the volcanic plumbing system beneath Tolbachik volcano (Kamchatka, Russia) revealed by long-period seismicity, *Earth Planet. Sci. Lett.* **493**, 47–56.
- Gallart, J., L. Driad, P. Charvis, M. Sapin, A. Hirn, J. Diaz, B. de Voogd, and M. Sachpazi (1999). Perturbation to the lithosphere along the hotspot track of La Réunion from an offshore-onshore seismic transect, *J. Geophys. Res.* **104**, no. B2, 2895–2908.
- Gerbault, M., F. J. Fontaine, M. Rabinowicz, and M. Bystricky (2017). Elastic flexure controls magma trajectories and explains the offset of primary volcanic activity upstream of mantle plume axis at La Réunion and Hawaii hotspot islands, *Earth Planet. Sci. Lett.* **462**, 142–156.
- Got, J.-L., V. Monteiller, J. Monteux, R. Hassani, and P. Okubo (2008). Deformation and rupture of the oceanic crust may control growth of Hawaiian volcanoes, *Nature* **451**, no. 7177, 453–456.
- Got, J.-L., A. Peltier, T. Staudacher, P. Kowalski, and P. Boissier (2013). Edifice strength and magma transfer modulation at piton de la Fournaise volcano, *J. Geophys. Res.* **118**, no. 9, 5040–5057.
- Gottsmann, J., L. Wooller, J. Martí, J. Fernández, A. G. Camacho, P. J. Gonzalez, A. Garcia, and H. Rymer (2006). New evidence for the reawakening of Teide volcano, *Geophys. Res. Lett.* **33**, no. 20, L20311, doi: [10.1029/2006GL027523](https://doi.org/10.1029/2006GL027523).
- Gualandi, A., C. Nichele, E. Serpelloni, L. Chiaraluze, L. Anderlini, D. Latorre, M. E. Belardinelli, and J.-P. Avouac (2017). Aseismic deformation associated with an earthquake swarm in the northern Apennines (Italy), *Geophys. Res. Lett.* **44**, no. 15, 7706–7714.
- Hainzl, S., T. Kraft, J. Wassermann, H. Igel, and E. Schmedes (2006). Evidence for rainfall-triggered earthquake activity, *Geophys. Res. Lett.* **33**, no. 19, L19303, doi: [10.1029/2006GL027642](https://doi.org/10.1029/2006GL027642).
- Hardebeck, J. L., and P. M. Shearer (2002). A new method for determining first-motion focal mechanisms, *Bull. Seismol. Soc. Am.* **92**, no. 6, 2264–2276.
- Harris, D. B. (2006). Subspace detectors: Theory, *Technical Report*, Lawrence Livermore National Laboratory, Livermore, California, doi: [10.2172/900081](https://doi.org/10.2172/900081).
- Hutton, L. K., and D. M. Boore (1987). The m_l scale in southern California, *Bull. Seismol. Soc. Am.* **77**, 2074–2094.
- Jacobs, K. M., and S. R. McNutt (2010). Using seismic b -values to interpret seismicity rates and physical processes during the pre-ruptive earthquake swarm at Augustine volcano 2005–2006, *U.S. Geol. Surv. Prof. Pap.*, 59 pp, doi: [10.3133/pp17693](https://doi.org/10.3133/pp17693).
- Jay, J. A., M. E. Pritchard, M. E. West, D. Christensen, M. Haney, E. Minaya, M. Sunagua, S. R. McNutt, and M. Zabala (2011). Shallow seismicity, triggered seismicity, and ambient noise tomography at the long-dormant Uturuncu volcano, Bolivia, *Bull. Volcanol.* **74**, 817–837.
- Kagan, Y. Y., and D. D. Jackson (1991). Long-term earthquake clustering, *Geophys. J. Int.* **104**, no. 1, 117–133.
- Kato, A., K. Obara, T. Igarashi, H. Tsuruoka, S. Nakagawa, and N. Hirata (2012). Propagation of slow slip leading up to the 2011 M_w 9.0 Tohoku-Oki earthquake, *Science* **335**, no. 6069, 705–708.
- Konstantinou, K. I., C.-H. Lin, and W.-T. Liang (2007). Seismicity characteristics of a potentially active Quaternary volcano: The Tatun volcano group, northern Taiwan, *J. Volcanol. Geotherm. Res.* **160**, 300–318.
- Kugaenko, Y., V. Saltykova, I. Koulakov, V. M. Pavlova, I. Abkadyrova, and V. Komzelevab (2021). An awakening magmatic system beneath the Udina volcanic complex (Kamchatka): Evidence from seismic unrest of 2017–2019, *Russian Geol. Geophys.* **62**, no. 3, 223–238.
- Lemarchand, N., and J.-R. Grasso (2007). Interactions between earthquakes and volcano activity, *Geophys. Res. Lett.* **34**, no. 24, 24303, doi: [10.1029/2007GL031438](https://doi.org/10.1029/2007GL031438).
- Lénat, J.-F., O. Merle, and L. Lespagnol (2009). La Réunion: An example of channeled hot spot plume, *J. Volcanol. Geotherm. Res.* **184**, nos. 1/2, 1–13.
- Lengliné, O., and D. Marsan (2009). Inferring the coseismic and postseismic stress changes caused by the 2004 $M_w = 6$ Parkfield earthquake from variations of recurrence times of microearthquakes, *J. Geophys. Res.* **114**, no. B10, doi: [10.1029/2008JB006118](https://doi.org/10.1029/2008JB006118).
- Lengliné, O., Z. Duputel, and V. Ferrazzini (2016). Uncovering the hidden signature of a magmatic recharge at Piton de la Fournaise volcano using small earthquakes, *Geophys. Res. Lett.* **43**, no. 9, 4255–4262.
- Lengliné, O., Z. Duputel, and P. G. Okubo (2021). Tracking dike propagation leading to the 2018 Kilauea eruption, *Earth Planet. Sci. Lett.* **553**, 116653, doi: [10.1016/j.epsl.2020.116653](https://doi.org/10.1016/j.epsl.2020.116653).
- Lin, C.-H. (2017). Dynamic triggering of volcano drumbeat-like seismicity at the Tatun volcano group in Taiwan, *Geophys. J. Int.* **210**, 354–359.
- Lohman, R. B., and J. J. McGuire (2007). Earthquake swarms driven by aseismic creep in the Salton trough, California, *J. Geophys. Res.* **112**, no. B4, doi: [10.1029/2006JB004596](https://doi.org/10.1029/2006JB004596).
- Lomax, A., A. Zollo, P. Capuano, and J. Virieux (2001). Precise, absolute earthquake location under Somma–Vesuvius volcano using a new three dimensional velocity model, *Geophys. Res. Lett.* **146**, no. 2, 313–331.
- Longpré, M.-A. (2021). Reactivation of Cumbre Vieja volcano, *Science* **374**, no. 6572, 1197–1198.
- Lopoukhine, M., and L. Stieltjes (1978). Evaluation du potentiel géothermique de île de La réunion-1ère phase exploratoire: Géologie et géochimie des eaux (no. 78 sgn 467 gth), *Technical Rept. BRGM*, available at <http://infoterre.brgm.fr/rapports/78-SGN-467-GTH.pdf> (last accessed September 2024) (in French).
- Marty, B., V. Meynier, E. Nicolini, E. Griesshaber, and J. Toutain (1993). Geochemistry of gas emanations: A case study of the Réunion Hot Spot, Indian Ocean, *Appl. Geochem.* **8**, 141–152.
- Matoza, R. S. (2020). Seismicity from the deep magma system, *Science* **368**, 708–709.

- McNutt, S. R. (1996). *Seismic Monitoring and Eruption Forecasting of Volcanoes: A Review of the State-of-the-Art and Case Histories*, Springer, Berlin, Heidelberg, 99–146.
- McNutt, S. R. (2005). Volcanic seismology, *Annu. Rev. Earth Planet. Sci.* **33**, no. 1, 461–491.
- Michon, L., V. Ferrazzini, and A. D. Muro (2016). Magma paths at Piton de la Fournaise volcano, in *Active Volcanoes of the Southwest Indian Ocean*, P. Bachèlery, J.-F. Lénat, A. D. Muro, and L. Michon (Editors), Springer-Verlag, Berlin, 91–106, doi: [10.1007/978-3-642-31395-0_7](https://doi.org/10.1007/978-3-642-31395-0_7).
- Michon, L., V. Ferrazzini, A. D. Muro, N. Villeneuve, and V. Famin (2015). Rift zones and magma plumbing system of Piton de la Fournaise volcano: How do they differ from Hawaii and Etna? *J. Volcanol. Geotherm. Res.* **303**, 112–129.
- Michon, L., F. Saint-Ange, P. Bachelery, N. Villeneuve, and T. Staudacher (2007). Role of the structural inheritance of the oceanic lithosphere in the magmato-tectonic evolution of Piton de la Fournaise volcano (La Réunion Island), *J. Geophys. Res.* **112**, no. B4, doi: [10.1029/2006JB004598](https://doi.org/10.1029/2006JB004598).
- Nadeau, R. M., and L. R. Johnson (1998). Seismological studies at Parkfield vi: Moment release rates and estimates of source parameters for small repeating earthquakes, *Bull. Seismol. Soc. Am.* **88**, no. 3, 790–814.
- Neal, C. A., S. R. Brantley, L. Antolik, J. L. Babb, M. Burgess, K. Calles, M. Cappos, J. C. Chang, S. Conway, L. Desmither, *et al.* (2019). The 2018 rift eruption and summit collapse of Kilauea volcano, *Science* **363**, no. 6425, 367–374.
- Nunez, D., F. J. Nunez-Cornu, and C. A. Rowe (2022). Recent seismicity at Ceboruco volcano (Mexico), *J. Volcanol. Geotherm. Res.* **421**, 107451, doi: [10.1016/j.jvolgeores.2021.107451](https://doi.org/10.1016/j.jvolgeores.2021.107451).
- Parsons, I. D., J. F. Hall, and G. A. Lyzenga (1988). Relationships between the average offset and the stress drop for two- and three-dimensional faults, *Bull. Seismol. Soc. Am.* **78**, no. 2, 931–945.
- Peltier, A., P. Bachèlery, and T. Staudacher (2009). Magma transport and storage at Piton de La Fournaise (La Réunion) between 1972 and 2007: A review of geophysical and geochemical data, *Geophys. Res. Lett.* **183**, nos. 1/2, 93–108.
- Peltier, A., F. Beauducel, N. Villeneuve, V. Ferrazzini, A. Di Muro, A. Aiuppa, A. Derrien, K. Jourde, and B. Taisne (2016). Deep fluid transfer evidenced by surface deformation during the 2014–2015 unrest at Piton de la Fournaise volcano, *J. Volcanol. Geotherm. Res.* **321**, 140–148.
- Rançon, J. (1985). Hydrothermal history of Piton des Neiges volcano (Réunion Island, Indian Ocean), *J. Volcanol. Geotherm. Res.* **26**, 297–315.
- Rançon, J., and P. Rocher (1985). Découverte de zones fumerolliennes récentes dans le cirque de Salazie (Ile de La Réunion, Océan Indien), *C. R. Geosci.* **300**, no. 16, 821–826.
- Richter, C. F. (1935). An instrumental earthquake magnitude scale, *Bull. Seismol. Soc. Am.* **25**, no. 1, 1–32.
- Romero, J. E., M. Burton, F. Cáceres, J. Taddeucci, R. Civico, T. Ricci, M. J. Pankhurst, P. A. Hernández, C. Bonadonna, E. W. Llewellyn, *et al.* (2022). The initial phase of the 2021 Cumbre Vieja ridge eruption (Canary Islands): Products and dynamics controlling edifice growth and collapse, *J. Volcanol. Geotherm. Res.* **431**, 107642, doi: [10.1016/j.jvolgeores.2022.107642](https://doi.org/10.1016/j.jvolgeores.2022.107642).
- Sapin, M., A. Him, J.-C. Lépine, and A. Nercressians (1996). Stress, failure and fluid flow deduced from earthquakes accompanying eruptions at Piton de la Fournaise volcano, *J. Volcanol. Geotherm. Res.* **70**, 145–167.
- Segall, P., E. K. Desmarais, D. Shelly, A. Miklius, and P. Cervelli (2006). Earthquakes triggered by silent slip events on Kilauea volcano, Hawaii, *Nature* **442**, no. 7098, 71–74.
- Sibson, R. H. (2014). Earthquake rupturing in fluid-overpressured crust: How common? *Pure Appl. Geophys.* **171**, 2867–2885.
- Sparks, R. S. J., J. Biggs, and J. W. Neuberg (2012). Monitoring volcanoes, *Science* **335**, no. 6074, 1310–1311.
- Ten Brink, U. S., and T. M. Brocher (1987). Multichannel seismic evidence for a subcrustal intrusive complex under Oahu and a model for Hawaiian volcanism, *J. Geophys. Res.* **92**, no. 13, 687–707.
- Traversa, P., and J.-R. Grasso (2010). How is volcano seismicity different from tectonic seismicity? *Bull. Seismol. Soc. Am.* **100**, no. 4, 1755–1769.
- Trugman, D. T., C. J. Chamberlain, A. Savvaidis, and A. Lomax (2023). Growclust3d.jl: A Julia package for the relative relocation of earthquake hypocenters using 3D velocity models, *Seismol. Res. Lett.* **94**, no. 1, 443–456.
- Uchida, N. (2019). Detection of repeating earthquakes and their application in characterizing slow fault slip, *Progr. Earth Planet. Sci.* **6**, no. 1, 40, doi: [10.1186/s40645-019-0284-z](https://doi.org/10.1186/s40645-019-0284-z).
- Vallée, M., J. Nocquet, J. Battaglia, Y. Font, M. Segovia, M. Régnier, P. Mothes, P. Jarrin, D. Cisneros, S. Vaca, *et al.* (2013). Intense interface seismicity triggered by a shallow slow slip event in the Central Ecuador subduction zone, *J. Geophys. Res.* **118**, no. 6, 2965–2981.
- Villeneuve, N., and P. Bachèlery (2006). Revue de la typologie des éruptions au Piton de la Fournaise, processus et risques volcaniques associés, *Eur. J. Geogr.* doi: [10.4000/cybergeog.2536](https://doi.org/10.4000/cybergeog.2536) (in French).
- Watts, A. B., and U. S. Ten Brink (1989). Crustal structure, flexure, and subsidence history of the Hawaiian Islands, *J. Geophys. Res.* **94**, no. 10, 473–500.
- Wech, A., W. Thelen, and A. Thomas (2020). Deep long-period earthquakes generated by second boiling beneath Mauna Kea volcano, *Science* **368**, no. 6492, 775–779.
- Wessel, P. (1993). A re-examination of the flexural deformation beneath the Hawaiian Islands, *J. Geophys. Res.* **98**, no. 12, 177–190.
- White, R., and W. McCausland (2016). Volcano-tectonic earthquakes: A new tool estimating intrusive volumes and forecasting eruptions, *J. Volcanol. Geotherm. Res.* **309**, 139–155.
- White, R., and W. McCausland (2019). A process-based model of pre-eruption seismicity patterns and its use for eruption forecasting at dormant stratovolcanoes, *J. Volcanol. Geotherm. Res.* **382**, 267–297.
- Wilding, J. D., W. Zhu, Z. E. Ross, and J. M. Jackson (2023). The magmatic web beneath Hawai'i, *Science* **379**, no. 6631, 462–468.
- Zhuang, J., D. S. Harte, M. J. Werner, S. Hainzl, and S. Zhou (2012). Basic models of seismicity: Temporal models, *Community Online Resource for Statistical Seismicity Analysis Theme V*, doi: [10.5078/corssa-79905851](https://doi.org/10.5078/corssa-79905851).

Manuscript received 16 November 2023

Published online 16 February 2024